

# 20x-Real Time Modeling and Simulation of More Electric Aircraft Thermally Integrated Electrical Power Systems

Yue Cao<sup>1</sup>, *Student Member, IEEE*, Matthew A. Williams<sup>2</sup>, *Student Member, IEEE*,  
Bradford J. Kearbey<sup>1</sup>, *Student Member, IEEE*, Andrew T. Smith<sup>1</sup>,  
Philip T. Krein<sup>1</sup>, *Fellow, IEEE*, Andrew G. Alleyne<sup>2</sup>, *Senior Member, IEEE*

**Abstract**—More electric aircraft (MEA) include higher power ratings and more power electronics than conventional aircraft. With electrification comes increased multi-physical interaction between power systems, especially in electrical and thermal domains. It is desirable to develop an accurate and fast system-level model that captures the dynamics of multiple energy domains over the course of candidate mission profiles, for the purpose of trade-off studies, prototyping, and controller development. This paper presents comprehensive electrical power component models that are capable of being assembled into full electrical system models. Steady-state and dynamic behaviors of electrical components including electric machines, power converters, batteries, transformers, and loads are captured by averaged switching modeling and  $dq0$  reference frame techniques, without sacrificing computational speed. An integrated thermal model within electrical components uses power loss calculations to model temperature variations and identify system hot spots. Monte Carlo simulation trials on a five-hour realistic mission establish the capability of the electrical system models while demonstrating a 50x real-time simulation speed for a standalone electric subsystem and 20x for a coupled electrical, thermal, and engine MEA model.

**Index Terms**—more electric aircraft (MEA), power systems, modeling and simulation, power electronics, electric machines, generators, loss modeling, thermal modeling

## I. INTRODUCTION

The most common more electric aircraft (MEA) architecture, which is already in commercial production on the Boeing 787, uses a no-bleed architecture, in which traditional pneumatic systems are replaced by electrically powered systems [1]. Environmental control systems (ECS) are no longer pneumatically powered, and instead the compressors, fans, and pumps are powered by electric motors via power electronics converters [2]. Due to this bleed-less architecture, maximum output of around 1.00 MVA comes from four engine-tied generators. With auxiliary power units (APU) for redundancy, a total of 1.45 MVA is installed on the Boeing 787 compared to 0.35 MVA on the Boeing 777 [2]. Increased electrical power introduces challenges due to coupled interactions between aircraft power systems, complexity due to additional electrical components, especially the power electronics and electric machines, and introduces more degrees of freedom for system control.

Major changes in the MEA electrical system include a variable voltage variable frequency 230 (nominal) Vac bus off the engine generators, a 270 Vdc bus and its attached motor driven loads, and an ac-dc-ac conversion from the 230 Vac bus to a regulated 400 Hz 115 Vac bus, as shown in Fig. 1 [3]. This configuration will be used throughout the paper and is the motivation for development of electrical component models

highlighted in Section II. Due to the large scale of these power systems, it is of great interest to rely on accurate modeling and simulation tools for design and prototyping. Two major categories of models exist: high-fidelity detailed switching models within electrical components [4], and system level averaged models that capture dynamical interaction between components [5][6]. This paper develops the latter. In particular, the average modeling method pertains to transforming three-phase  $abc$  ac signals into a synchronous rotating  $dq0$  frame. Such technique has been proved effective in accuracy and speed in electric power systems of mobile applications [5][7]. Recently a dynamic phasor method [8] has been developed to enhance the  $dq0$  approach and address unbalanced fault conditions. This method will not be applied in this paper, however, as a balanced three-phase situation is to be explored for mission energy trade-offs.

Additionally, it is important to understand and capture the thermal behavior of electrical system components in order to avoid failures due to overheating and thermal runaway. A suitable thermal model is necessary for hot spot detection and temperature monitoring. The combined electrical-thermal model must run fast while capturing necessary dynamics. Thermal models usually have step sizes of milliseconds or slower, whereas electrical models that capture switching behaviors have step sizes of milliseconds or faster. Therefore, switch level models are not suitable when considering system-level simulations. An averaged switching modeling approach is able to capture power losses in power electronic converters and batteries, including device conduction and switching losses, based on equivalent steady-state conditions [9][10]. Transient dynamics in the generators are captured using d-q models that execute with millisecond or faster time steps [9][11]. Previous work [9][12] has tackled the above modeling goals in part. However, [9] focuses on power system faults, and [12] is heavy on mechanical design. Neither addresses electrical component thermal modeling. In this paper, the above criteria will be met. Simulation time versus real time will be measured to demonstrate the computation speed.

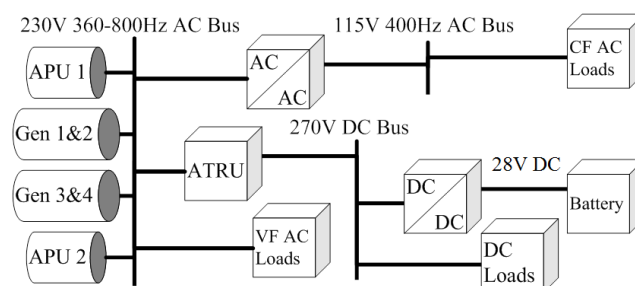


Fig. 1. Boeing 787 electrical power system architecture (recreated from [3]).

<sup>1</sup>Yue Cao, Bradford J. Kearbey, Andrew T. Smith, and Philip T. Krein are with the Department of Electrical and Computer Engineering, University of Illinois, Urbana-Champaign, IL 61801, USA (email: yuecao2@illinois.edu, kearbey2@illinois.edu, atsmith3@illinois.edu, krein@illinois.edu).

<sup>2</sup>Matthew A. Williams and Andrew G. Alleyne are with the Department of Mechanical Science and Engineering, Univ. of Illinois, Urbana-Champaign, IL 61801, USA (email: mwillms4@illinois.edu, alleyne@illinois.edu).

In Section II, electrical and thermal models for individual MEA components are developed. Section III combines these models into two simulation platforms: 1) electrical system in isolation, 2) MEA system architecture with electrically driven ECS and engine power generators. Section IV provides the

results of 1000 Monte Carlo simulations on simulation speeds, electrical system bus voltages, and total generated power.

## II. ELECTRICAL POWER SYSTEM MODELING

In this section, the main building blocks of aircraft electrical power systems including generators, exciters, power converters, battery cells, transformers, and electrical loads will be explained, and modeling details will be presented.

Electrical load distributions and power conversion efficiencies in the Boeing 787 at a typical cruising condition are described in Fig. 2 [13]. This chart provides scaling information for modeling development as well as sanity check data for simulation results. The electrical power system contains the exciter/generator and APU connected to the electrical distribution system. Electrical component models incorporate power loss calculation, which affects the component temperature, and are coupled to ECS models that handle heat rejection due to electrical losses. Engine models provide low-pressure spool speeds and receive load torque from generators. Fig. 3 shows signal flow from the electrical system to the engine (black lines) and to the thermal system (red lines). The green lines show the dependency of other systems on electrical power.

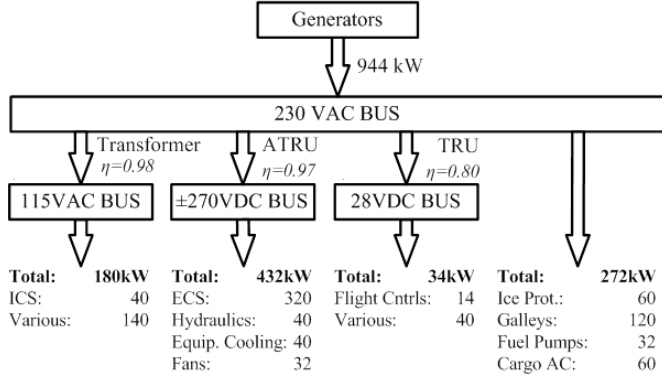


Fig. 2. Typical electrical system loads and efficiencies at cruise condition in Boeing 787 (recreated from [13]).

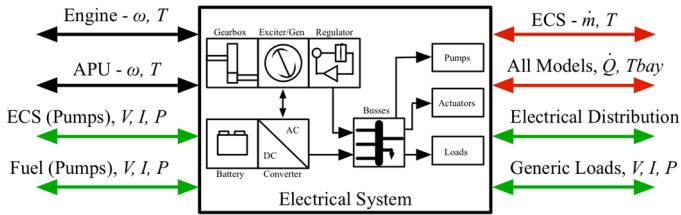


Fig. 3. Electrical power system diagram with input/output dependencies.

### A. Generator

The generator consists of a synchronous generator, a synchronous exciter, and exciter controls. The input/output structure is shown in Fig. 4. The engine speed serves as an input, and is adjusted based upon a fixed gear ratio. A dc voltage input provides voltage potential to the exciter, and load currents in the  $dq0$  reference frame impose the total current load on the generator. The mathematical model outputs provide a  $dq0$  line voltage from the generator, current draw by the exciter system, a torque on the engine, and heat produced due to losses. The synchronous generator and exciter models will be detailed in this paper. The input/output structure of a wound-field synchronous generator is shown in Fig. 5.

#### 1) Electrical Model

In ac machine models, sinusoidal states can lead to computationally intensive simulations. Alternatively, a well-known synchronous, or direct-quadrature-zero (dq0) reference

frame, can be used. Sinusoidal states are transformed using Park's transformation [14], which results in constant steady-state conditions, larger solver time steps, and faster simulations. The following generator model is derived in the  $dq0$  reference frame. Parameter values are dependent upon specific machines; however, [15] contains examples of various machines and their respective parameters, which can be used as a baseline for sizing the generator.

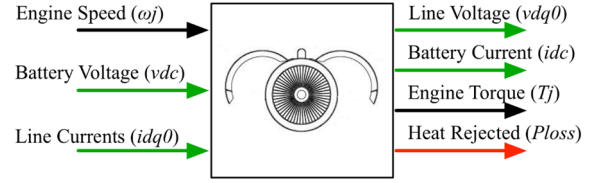


Fig. 4. Generator system inputs/outputs.

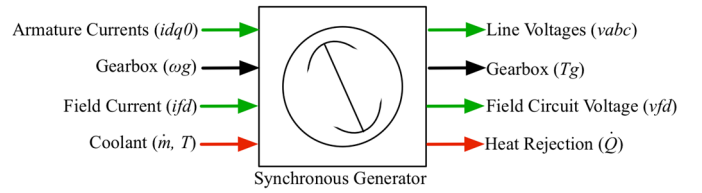


Fig. 5. Synchronous generator inputs and outputs.

Denoting the direct axis with subscript  $d$  and the quadrature axis with subscript  $q$ , the electromotive force  $E'$  dynamics for the stator are modeled as

$$\frac{T'_{do}}{k} \frac{dE'_q}{dt} = -E'_q - (X'_d - X''_d) \left[ I_d - \frac{X'_d - X''_d}{(X'_d - X'_s)^2} (\psi_{1d} + (X'_d - X'_s) I_d - E'_q) \right] + E_{fd} \quad (1)$$

$$\frac{T'_{qo}}{k} \frac{dE'_d}{dt} = -E'_d + (X'_q - X''_q) \left[ I_q - \frac{X'_q - X''_q}{(X'_q - X'_s)^2} (\psi_{2q} + (X'_q - X'_s) I_q + E'_d) \right] \quad (2)$$

where  $X$  is the per-unit reactance,  $X'$  is the per-unit transient reactance,  $X''$  is the per-unit sub-transient reactance,  $X'_s$  is the leakage reactance,  $T'_{do}$  and  $T'_{qo}$  are the per-unit transient field winding time constants in their respective axes, and  $I$  is the current [11].

The flux linkage  $\psi$  dynamics are defined as

$$\frac{T''_{do}}{k} \frac{d\psi_{1d}}{dt} = -\psi_{1d} + E'_q - (X'_d - X'_s) I_d \quad (3)$$

$$\frac{T''_{qo}}{k} \frac{d\psi_{2q}}{dt} = -\psi_{2q} - E'_d - (X'_q - X'_s) I_q \quad (4)$$

where  $T''_{do}$  and  $T''_{qo}$  are the sub-transient field winding time constants in their respective axes [11].

The effect of temperature on electromotive force is captured by considering the change in electrical resistance due to temperature. The coefficient  $k$  in (1)-(4) is defined as

$$k = \frac{R(T)}{R(T_0)} = 1 + \alpha \Delta T \quad (5)$$

where  $\Delta T$  is the temperature difference between the generator temperature  $T$  and the nominal temperature  $T_0$ , and  $\alpha$  is the coefficient of resistance for the field coil windings (for copper,  $\alpha = 3.85 \times 10^{-3}$ ).

The scaled field voltage  $E_{fd}$  is defined as

$$E_{fd} = \frac{I_{fd} X_{md}}{S_B} V_B \quad (6)$$

where  $X_{md}$  is the direct axis magnetizing reactance,  $I_{fd}$  is the direct axis field current,  $S_B$  is the base generator power which is equal to the rated three-phase volt-amperes, and  $V_B$  is base generator voltage. The field current is supplied by the exciter system, and is detailed in the following section.

Voltages in  $d$  and  $q$  axes can be calculated as algebraic functions of the electromotive forces, currents, and flux linkages,

$$V_q = -\omega(X_d'' + X_{TL})I_d - (kR_s + R_{TL})I_q + \omega \left( E_q' \frac{X_d'' - X_{Ls}}{X_d' - X_{Ls}} + \psi_{1d} \frac{X_d' - X_d''}{X_d' - X_{Ls}} \right) \quad (7)$$

$$V_d = \omega(X_q'' + X_{TL})I_q - (kR_s + R_{TL})I_d + \omega \left( E_d' \frac{X_q'' - X_{Ls}}{X_q' - X_{Ls}} + \psi_{2q} \frac{X_q' - X_q''}{X_q' - X_{Ls}} \right) \quad (8)$$

where  $X_{TL}$  and  $R_{TL}$  are the line reactance and resistance,  $\omega$  is the rotational speed, and  $R_s$  is the stator resistance.

Electromagnetic torque  $T_{EM}$  of the generator is calculated in

$$T_{EM} = \psi_d'' I_q - \psi_q'' I_d \quad (9)$$

where

$$\psi_d'' = \left( \frac{X_d'' - X_{Ls}}{X_d' - X_{Ls}} \right) E_q' + \left( \frac{X_d' - X_d''}{X_d' - X_{Ls}} \right) \psi_{1d} \quad (10)$$

$$\psi_q'' = \left( \frac{X_q'' - X_{Ls}}{X_q' - X_{Ls}} \right) E_d' + \left( \frac{X_q' - X_q''}{X_q' - X_{Ls}} \right) \psi_{2q} \quad (11)$$

Power losses due to inefficiencies are determined as

$$P_{loss} = S_B \left( \frac{P}{2} \omega T_{EM} - E_d I_d - E_q I_q \right) \quad (12)$$

where  $P$  is the number of pole pairs. Power loss is essentially the difference between the shaft input power and the electrical output power.

## 2) Thermal Model

A lumped thermal capacitance model is used to represent the overall temperature of the generator. Temperature is affected by losses from (12) and heat transfers between the generator and ambient air as well as between the generator and coolant. The time rate of change of the generator temperature,  $T_{gen}$ , is

$$m_{gen} C_{p,gen} \frac{dT_{gen}}{dt} = P_{loss} + h_f A_f (T_f - T_{gen}) + h_a A_a (T_a - T_{gen}) \quad (13)$$

where  $m_{gen}$  is the mass of the generator,  $C_{p,gen}$  is the specific heat of the generator lumped thermal capacitance,  $A_a$  is the heat transfer area between the ambient air and the generator, and  $A_f$  is the heat transfer area between the coolant flow and the generator. Each heat transfer coefficient  $h$  is calculated using the Nusselt number  $Nu$ , the thermal conductivity of the fluid  $k$ , and the length over which the heat transfer occurs, by

$$h = Nu \frac{k}{L} \quad (14)$$

The Nusselt number for the coolant flowing through the generator is calculated assuming turbulent pipe flow and the Gnielinski correlation [16]. Similarly, the Nusselt number for the air moving over the generator assumes turbulent flow over a cylinder, which can be calculated using the Churchill-Bernstein correlation [16].

## B. Exciter

The synchronous machine described above requires a field current supply. Commonly another wound-field or permanent magnet synchronous generator, known as an exciter, coupled to the main generator shaft provides this current. The exciter's output terminals are rectified and directly connected to the main generator field terminals. This field current must be provided independent of the generator and should be controlled properly to regulate the generator terminal voltage. A battery provides the exciter's field current, regulated through a dc/dc converter. A generic structural diagram is shown in Fig. 6.

The mathematical model of the exciter is identical to the model provided in the previous generator's subsection. A generic exciter controller mathematical model will be provided here. The field-controller converter duty cycle ( $m$ ) is obtained from

$$\dot{r} = k_1 (V_{ref} - V_{line}(t)) \quad (15)$$

$$\dot{m} = k_2 (r - k_3 m) \quad (16)$$

$$V_{line}(t) = \sqrt{v_d^2 + v_q^2} \quad (17)$$

where  $k_1$ ,  $k_2$ , and  $k_3$  are controller gains,  $r$  is an arbitrary variable, and  $m$  is the dc/dc converter duty ratio. The reference line voltage is  $V_{ref}$  and the measured line voltage is  $V_{line}$ .

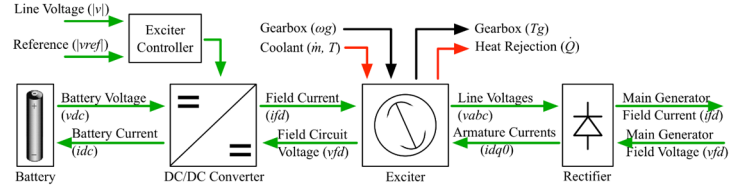


Fig. 6. Exciter block diagram and signal flow.

## C. Inverter

### 1) Electrical Model

The three-phase inverter block converts the dc bus voltage to ac voltage, which interfaces with the rest of the ac system directly or through a transformer. Since the inverter is modeled in the  $dq0$  reference frame, the inverter output voltages become constant values in steady state due to the  $abc$ - $dq0$  transformation. An averaged switching power loss modeling technique is used to ensure fast simulation [17]. The conduction loss is incurred when the IGBT (or equivalent) is on. It can be modeled as an ideal switch in series with a forward voltage drop  $V_{on}$  and a series resistor  $R_{ds}$ .  $V_{on}$  and  $R_{ds}$  can be obtained directly from the IGBT datasheet. The average conduction loss per IGBT pair is

$$P_{on\_inv} = \frac{2\sqrt{2}I_{rms}V_{on}}{\pi} + I_{rms}^2 R_{ds} \quad (18)$$

The averaged switching loss of each IGBT pair can be estimated as

$$P_{switch\_inv} = \frac{2\sqrt{2}I_{rms}V_{bus}}{\pi} f_{switch\_inv} \frac{t_{on} + t_{off}}{2} \quad (19)$$

where  $f_{switch\_inv}$  is the inverter switching frequency. Times  $t_{on}$  and  $t_{off}$  are the switching rise and fall times, respectively, which are also found in device datasheet.  $V_{bus}$  is the main dc bus voltage.

Another input needed to control the three-phase inverter is switching functions. However, since the inverter is an averaged model in the  $dq0$  frame, the switching functions  $q$  that determine direct action of the switching devices are replaced with modulating functions [18]. When sinusoidal pulse width modulation method is used to control the inverter switches, the output line-line (rms) voltage of the inverter is given as

$$V_{l-l(rms)} = \sqrt{\frac{3}{2}} q V_{dc} \quad (20)$$

The modulating functions for the three-phase inverter become voltage rms magnitudes. The phase of the inverter output voltages with respect to the rest of the ac system can be changed by modifying relative values in the  $d$  and  $q$  axis controls.

### 2) Thermal Model

A lumped thermal capacitance model is used to represent the overall temperature of the inverter. It is assumed that the

inverter is cooled under natural convection from a finned surface in an electronics bay at temperature  $T_{bay}$ . The rate of change of the inverter temperature,  $T_{inv}$ , is

$$m_{inv} C_{p,inv} \frac{dT_{inv}}{dt} = P_{on\_inv} + P_{switch\_inv} + h(2nLH)(T_{bay} - T_{inv}) \quad (21)$$

where  $m_{inv}$  is the mass of the inverter and heat sink, and  $C_{p,inv}$  is the specific heat of the inverter lumped capacitance. The last term is the heat transfer due to an  $n$ -finned heat sink with fins that are  $H$  meters tall and  $L$  meters long. The heat transfer coefficient  $h$  is calculated as

$$h = 1.31 \frac{k}{S_{opt}} \quad (22)$$

where  $k$  is the thermal conductivity of the fins. The optimal fin spacing  $S_{opt}$  for a vertical heat sink is given by the Rohsenow and Bar-Cohen correlation [16] and is a function of the Rayleigh Number  $Ra$  and the length  $L$  of the fins

$$S_{opt} = 2.714 \frac{L}{Ra^{1/4}} \quad (23)$$

#### D. Rectifier

The rectifier block converts ac voltage to dc voltage, which interfaces with the rest of the dc system. This is an active rectifier and it is modeled in the synchronous  $dq0$  reference frame. A voltage-based model is implemented and a dc-link inductor is assumed. The rectifier is modeled as:

$$L \frac{di_{out}}{dt} = m \cdot V_{line}(t) - V_{out} \quad (24)$$

$$\theta = \arctan\left(\frac{v_q}{v_d}\right) \quad (25)$$

$$i_q = m \cdot i_{out} \cdot \sin(\theta) \quad (26)$$

$$i_d = m \cdot i_{out} \cdot \cos(\theta)$$

where  $V_{out}$  is the output dc voltage,  $i_{out}$  is the output dc current, and  $m$  is the modulation depth.

Power loss is modeled in a similar fashion as it is in the inverter model [17], since the topology of the rectifier is a mirror image of the inverter. Similar thermal models used for the inverter are also implemented.

#### E. Battery

##### 1) Battery Electrical Model

This subsection deals with the implementation of a lithium-ion battery and its mathematical model. In the following model, battery parameters are determined from laboratory tests on a sample lithium-ion battery (Panasonic CGR18650A). The model itself is generic and can be adapted for a wide range of batteries, including Li-ion, NiMH and lead-acid batteries. However, the battery circuit model parameters must be estimated using a battery testing procedure [19]. The battery capacity is a function of the charge/discharge rates  $i(t)$ , temperature  $T(t)$  and cycle number  $n_{cycle}$  and a rate factor  $f(i(t))$  which is a function of current. The rate factor is used to account for undesired side reactions with increase with current magnitude. The dynamic capacity of the battery represented by its state of charge (SOC) is a function of these factors and given by

$$\begin{aligned} SOC(t) &= SOC_{initial} - \int_0^t f_1[i(t)] \cdot f_2[T(t)] \cdot f_3[n_{cycle}] \cdot i(t) \cdot \frac{1}{\zeta} dt \\ &\quad - \int_0^t i_{self-discharge} \cdot \frac{1}{\zeta} dt \\ &\approx SOC_{initial} - \int_0^t f_1[i(t)] \cdot f_2[T(t)] \cdot f_3[n_{cycle}] \cdot i(t) \cdot \frac{1}{\zeta} dt \end{aligned} \quad (27)$$

The battery is modeled using the notion of multiple scaled time constants, each at a level such as seconds, minutes and hours. In the electrical equivalent circuit, each time constant can be modeled as a resistance-capacitance combination, as shown in Fig. 7. Measurements of the circuit parameters are found by using a battery testing apparatus and recording the test sequences and data corresponding to open circuit voltage ( $V_{oc}$ ) and terminal voltage ( $V_t$ ) versus SOC at multiple ambient temperatures. Each parameter (resistance and capacitance) in the model shown in Fig. 7 is a nonlinear function of SOC. For a practically useable model, in [19] each parameter is represented as a polynomial function of the SOC up to sixth order given as

$$V, R, C = \exp\left[\sum_{k=0}^6 a_k \ln^k(SOC)\right] \quad (28)$$

The coefficients  $a_0$ - $a_6$  (exact values can be found in [19]) are obtained by a best-fit polynomial expression on the experimentally determined data points. From the equivalent circuit, the battery terminal voltage can be calculated as implemented in fast frequency domain,

$$V_t = V_{oc} - i \cdot \left( R_{series} + R_{sec} \parallel \frac{1}{sC_{sec}} + R_{min} \parallel \frac{1}{sC_{min}} + R_{hour} \parallel \frac{1}{sC_{hour}} \right) \quad (29)$$

In addition, a temperature model is developed by

$$mc \frac{dT(t)}{dt} = i^2(t) R_{series} + \frac{V_{sec}^2(t)}{R_{sec}} + \frac{V_{min}^2(t)}{R_{min}} + \frac{V_{hour}^2(t)}{R_{hour}} - h_c A [T(t) - T_a] \quad (30)$$

Mass,  $m$ , external surface area,  $A$ , and specific heat,  $c$ , are inherent battery properties. Applications and thermal designs determine the ambient temperature,  $T_a$ , and heat transfer coefficient,  $h_c$ .

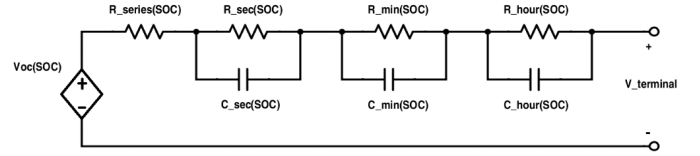


Fig. 7. Electrical equivalent circuit of the battery model [19].

#### F. Transformer

The transformer block converts the primary winding voltage level or provides galvanic insulation. A steady-state electrical model is implemented. Only resistive voltage drops are included and reactances are neglected. The model is flexible and can be used as a single-phase or multi-phase transformer interchangeably. The inputs and outputs are in the synchronous reference frame. The magnetic coupling is ideal and only copper losses are modeled. The input-output electrical relation is

$$\frac{(V_p - i_p R_p)}{(V_s - i_s R_s)} = \frac{N_p}{N_s} \quad (31)$$

where  $V_p$  and  $V_s$  are primary winding and secondary winding voltages,  $i_p$  and  $i_s$  are primary winding and secondary winding currents, and  $N_p$  and  $N_s$  are primary and secondary windings number of turns, respectively.

#### G. Electrical Loads

The electrical loads are classified into varying power, current or impedance loads to model different user requirements. These loads are also modeled in the  $dq0$  reference frame. The loads are modeled as lumped quantities. Assuming a balanced three-phase system, the zero axis electrical quantities are zero in steady state and need not be tracked.

### III. SIMULATION RESULTS

A five-hour flight (or mission) profile is used to test the modeled electrical system. Electrical load magnitudes are based on Boeing 787 total electrical loading variations documented in [13]. Fig. 8 shows total electrical loads on all generators for various flight phases under maximum ice conditions. With the Boeing 787 having 1 MVA installed generator power, these conditions are near maximum operational capability. Using Fig. 2 and Fig. 8 as reference, a customized baseline electrical loading profile is generated for this 5-hour flight, as shown in Fig. 9. Electrical loads are broken into 28 Vdc, 270 Vdc, 230 Vac, and 115 Vac subunits. For the purpose of mismatched generator loading tests, it is assumed that generators 1 & 2 support loads on the 230 Vac and 115 Vac busses, while generators 3 & 4 support loads on the 230 Vac, 270 Vdc, and 28 Vdc busses, as shown in Fig. 10. Furthermore, during the second half of the flight total power levels decrease as galley and cabin loads are turned off.

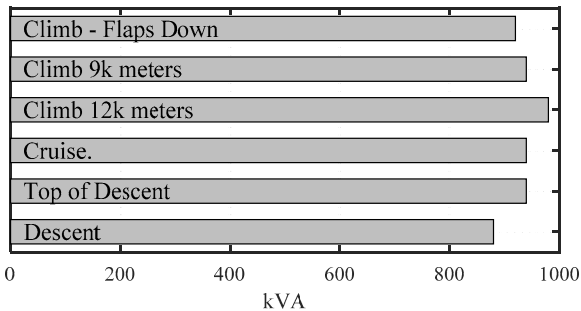


Fig. 8. Total electrical loads on Boeing 787 generators during major flight segments with maximum ice conditions [13].

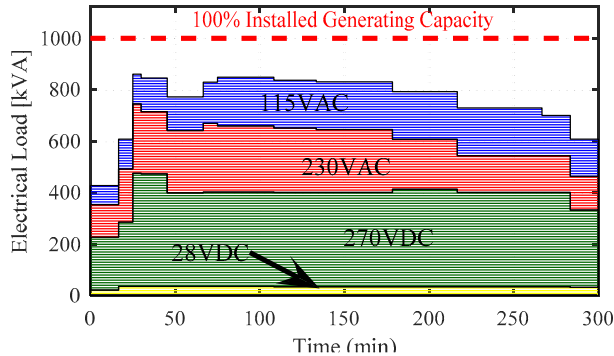


Fig. 9. Electrical loads on each voltage bus over a 5-hour flight.

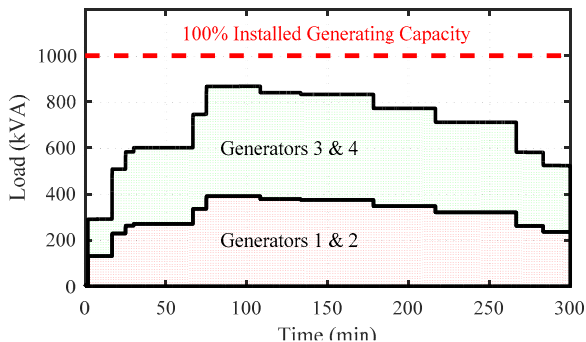


Fig. 10. Total load on each set of generators for the 5-hour flight.

Two sets of simulation studies are conducted: 1) isolated electrical system with fixed boundary conditions, 2) coupled electrical, thermal, and engine system simulations. In the isolated system simulations, boundary conditions such as generator thermal management, electrical loads, and engine speeds are fixed *a priori*. This means that there is no dynamic feedback between the electrical system and the thermal management or engine systems. In the coupled simulations, full dynamic feedback is included.

In total, 1000 simulations are run for each set of studies (isolated and coupled electrical system). Each Monte Carlo case is constructed as follows: 1) Random weights in a uniform distribution with maximum  $\pm 10\%$  magnitude changes are assigned to each portion of the baseline profile in Fig. 9; 2) Random time variation at an interval of 1 s and within the range of 5% in magnitude is imposed on the 270 Vdc load to produce time variability to each test case. Each case is tested first with only the electrical subsystem and next with a fully coupled simulation. For each simulation, a real time ratio (*RTR*) is calculated by

$$RTR = \frac{\text{Simulation Time}}{\text{Elapsed Real Time}} \quad (32)$$

The *RTR* demonstrates how much faster the simulation executes compared to real time and is sensitive to transients as well as noise in signals that are integrated. Fig. 11 shows the frequency of the *RTR* over 1000 simulations of the isolated electrical system. On average,  $RTR=48.3$ , meaning that a 5-hour flight can be simulated in  $\sim 6$  minutes. The *RTR* decreases, averaged at 22.1, when dynamic models of the complete system are considered, as seen in Fig. 12.

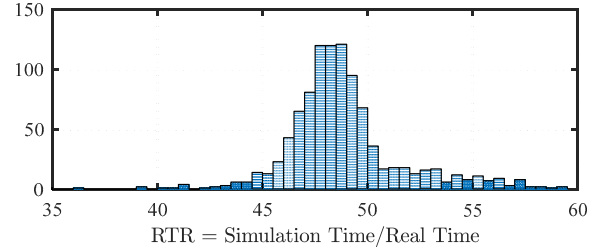


Fig. 11. Frequency of various *RTR* occurring for a simulated flight profile of the isolated electrical system.

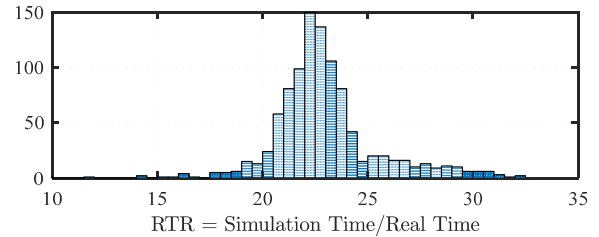


Fig. 12. Frequency of various real time ratios (*RTR*) occurring for a simulated flight profile of the electrical system coupled to thermal management and engine systems.

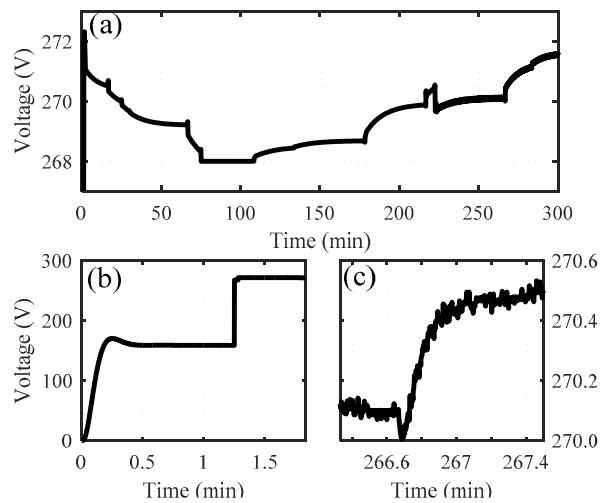


Fig. 13. Voltage at the 270 Vdc bus: (a) full profile of bus voltage over the 5-hour flight, (b) detail showing bus voltage during generator start up, (c) detail showing voltage noise during high load conditions.

Fig. 13 shows the 270 Vdc bus for the baseline Monte Carlo case. In (a), the voltage of the bus over the course of the flight is shown. Controllers integrated into the ATRU keep the

voltage between 268-272 V for the duration of the flight. In (b), the bus voltage during generator start-up is shown. Shortly after 1 minute, the ATRU control routine is switched on to bring the bus to 270 Vdc. In (c), detail of the noise on the bus due to ECS and hydraulics loads is shown. Fig. 14 shows the q-voltage on the 230 Vac bus. Notice that the 230 Vac bus also has a d-voltage as part of the  $dq0$  transformation.

Generator temperatures over the course of the simulation are shown in Fig. 15 for the same Monte Carlo case as in Fig. 14. Due to asymmetric loading between the pairs of generators, temperatures over the flight vary slightly. No active control of the thermal management system for the generators is included in these results, thus the generator temperatures are allowed to fluctuate significantly over the course of the simulation. With the inclusion of the thermal management system [12] the generator temperature can be kept within set thermal constraints.

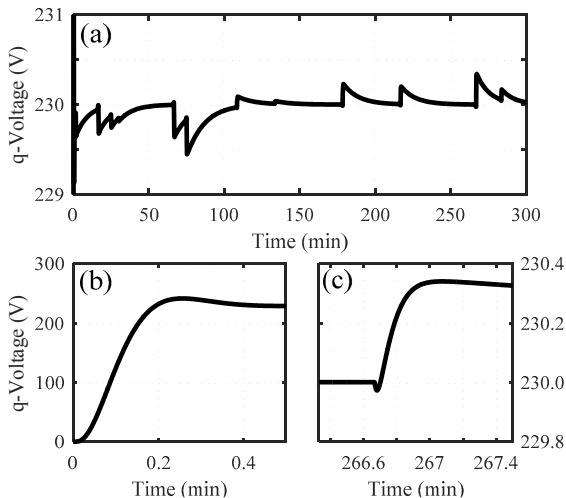


Fig. 14. Voltage at the 230 Vac bus: (a) full profile of bus voltage over the 5-hour flight, (b) detail showing bus voltage during generator start up, (c) detail showing voltage during high load conditions, without the noise from the dc loads in Fig. 13.

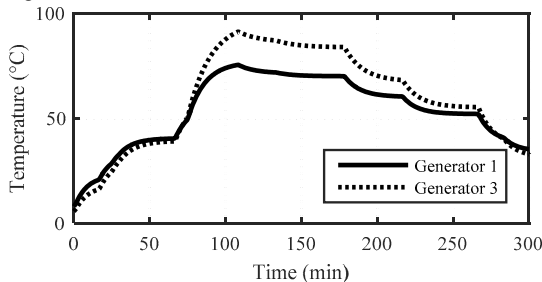


Fig. 15. Generators 1 and 3 temperature profiles over the 5-hour flight.

#### IV. CONCLUSIONS

This paper presents a comprehensive electrical power system model for MEA, with integrated component thermal behavior prediction. The major electrical components including generators, power converters, batteries, transformers, and loads preserve necessary voltage, current, and power details with  $dq0$  reference frame and averaged switching modeling techniques. Thermal models, useful for temperature monitoring and hot spot detection, are included for generators, power converters, and batteries. The isolated electrical subsystem runs at approximately 50 times real-time speed, and 20 times for the fully integrated electrical-thermal-engine aircraft system. Simulation results show robust waveform behaviors at 230 Vac and 270 Vdc buses. Future work includes possible experimental verification for an electric power system given a scaled down mission profile.

#### ACKNOWLEDGMENTS

This work was supported by Rolls-Royce Corporation. The authors would like to acknowledge their support and guidance in developing the models.

#### REFERENCES

- [1] M. Sinnett, "787 No-Bleed Systems: saving fuel and enhancing operational efficiencies," *Boeing Aero*, vol. 4, pp. 6–11, 2007.
- [2] B. Sarlioglu and C. T. Morris, "More electric aircraft: review, challenges, and opportunities for commercial transport aircraft," *IEEE Trans. Transportation Electrification*, vol. 1, no. 1, pp. 54–64, 2015.
- [3] X. Zhao, J. M. Guerrero, and X. Wu, "Review of aircraft electric power systems and architectures," in *Proc. IEEE International Energy Conf.*, 2014, pp. 949–953.
- [4] A. Davoudi, J. Jatskevich, P. L. Chapman, and A. Bidram, "Multi-resolution modeling of power electronics circuits using model-order reduction techniques," *IEEE Trans. Circuits and Systems I: Regular Papers*, vol. 60, no. 3, pp. 810–823, 2013.
- [5] S. V. Bozhko, T. Wu, C. I. Hill, and G. M. Asher, "Accelerated simulation of complex aircraft electrical power system under normal and faulty operational scenarios," in *Proc. IEEE Industrial Electronics Society Conf.*, 2010, pp. 333–338.
- [6] S. Chiniforoosh, J. Jatskevich, A. Yazdani, et al., "Definitions and applications of dynamic average models for analysis of power systems," *IEEE Trans. Power Delivery*, vol. 25, no. 4, pp. 2655–2669, 2010.
- [7] S. R. Sanders, J. M. Noworolski, X. Z. Liu, and G. C. Verghese, "Generalized averaging method for power conversion circuits," *IEEE Trans. Power Electronics*, vol. 6, no. 2, pp. 251–259, 1991.
- [8] T. Yang, S. Bozhko, and G. Asher, "Fast functional modelling of diode-bridge rectifier using dynamic phasors," *IET Power Electronics*, vol. 8, no. 6, pp. 947–956, 2015.
- [9] C. Mak, S. Sridharan, and P. T. Krein, "Fault Modeling and Simulation for More-Electric Aircraft Systems," in *Proc. IEEE Workshop on Control and Modeling for Power Electronics (COMPEL)*, 2015.
- [10] Y. Cao and P. T. Krein, "An average modeling approach for mobile refrigeration hybrid power systems with improved battery simulation," in *Proc. IEEE Transportation Electrification Conf. (ITEC)*, 2013.
- [11] P. C. Krause, O. Wasynczuk and S. D. Sudhoff, *Analysis of Electric Machinery and Drive Systems*, IEEE Press, 2002.
- [12] M. Williams, S. Sridharan, S. Banerjee, C. Mak, C. Pauga, P. T. Krein, A. Alleyne, A. Jacobi, and S. D'Urso, "PowerFlow: a toolbox for modeling and simulation of aircraft systems," in *Proc. SAE AeroTech Congress & Exhibition*, 2015.
- [13] G. A. Whyatt and L. A. Chick, "Electrical generation for more electric aircraft using solid oxide fuel cells," Pacific Northwest National Laboratory, Richland, Washington, Tech. Rep. PNNL-21382, April 2012.
- [14] P.M. Anderson and A.A. Fouad, *Power System Control and Stability*, 1<sup>st</sup> ed., IEEE Press, 2003.
- [15] P. W. Sauer and M. A. Pai, *Power System Dynamics and Stability*, Prentice Hall Press, 1998.
- [16] F. Incropera, D. DeWitt, *Fundamentals of Heat and Mass Transfer*, 6<sup>th</sup> Ed., New York, Wiley, 2007, pp 490–515.
- [17] Y. Cao and P. T. Krein, "Average and detailed modeling approaches emphasizing subsystems in a hybrid mobile refrigeration," in *Proc. IEEE International Electric Machines and Drives Conf. (IEMDC)*, 2013, pp. 1132–1136.
- [18] P. T. Krein, *Elements of Power Electronics*, 2<sup>nd</sup> ed. New York: Oxford University Press, 2015.
- [19] Y. Cao, R. C. Kroeze, and P. T. Krein, "Multi-timescale parametric electrical battery model for use in dynamic electric vehicle simulations," *IEEE Trans. Transportation Electrification*, vol.2, no. 4, 2016.